

Significant surface transport in topological insulator  $\text{Bi}_{1.5}\text{Sb}_{0.5}\text{Te}_{1.8}\text{Se}_{1.2}$   
single crystalline nanoflake device

Bin Xia<sup>1</sup>, Peng Ren<sup>1</sup>, Azat Sulaev<sup>1</sup>, Shi Chen<sup>1</sup>, Cesare Soci<sup>1</sup>, Xiaojiang Yu<sup>3</sup>, Hongwei  
Ou<sup>3</sup>, Alfred Huan<sup>1</sup>, Andrew TS Wee<sup>2</sup>, Andriwo Rusydi<sup>2,3</sup>, Shun-Qing Shen<sup>4</sup>, Lan  
Wang<sup>1\*</sup>

1. *School of Physical and Mathematical Science, Nanyang Technological University, Singapore, 637371, Singapore*
2. *Department of Physics, National University of Singapore, Singapore 117542, Singapore*
3. *NUSNNI-NanoCore, Singapore Synchrotron Light Source, National University of Singapore, Singapore 117603, Singapore*
4. *Department of Physics, The University of Hong Kong, Pokfulam Road, Hong Kong, People's Republic of China*

We report experimental evidence of significant surface transport in single crystalline nanoflake devices of 200 nm thick topological insulator  $\text{Bi}_{1.5}\text{Sb}_{0.5}\text{Te}_{1.8}\text{Se}_{1.2}$ . The resistivity measurements show dramatic difference between nanoflake device and bulk single crystal in which the nanoflake device shows a transition from semiconductor to metal at  $\sim 100$  K with decreasing temperature, while the bulk single crystal shows only semiconductor behavior in the measured temperature range from 300 K to 10 K. Angle-dependent magneto-resistance curves of the nanoflake devices are fitted to a universal curve when the x-axis is the perpendicular component of the applied magnetic field. Furthermore, the temperature dependence of magneto-conductance of the 200 nm thick ( $>$  the phase breaking length) nanoflake device presents two-dimensional behaviors of weak antilocalization. Moreover, the time dependent universal conductance fluctuation strongly indicates two-dimensional surface transport. Our result open a path for realization of novel electric and spintronic device based on the topological helical surface states.

\*Email: wanglan@ntu.edu.sg

PACS numbers: 73.25.+i, 73.20.Fz, 72.20.My, 73.23.-b

Topological insulators (TIs) are gapped bulk insulators with gapless Dirac surface states [1-4]. The surface states of these topological insulators are spin polarized and protected by time-reversal symmetry. A number of surface spectroscopy measurements, such as spin and angle-resolved photoemission spectroscopy (ARPES) [5-13] and scanning tunneling microscopy [14, 15], has been used to detect the topologically nontrivial surface state in three-dimensional topological insulator  $\text{Bi}_{1-x}\text{Sb}_x$ ,  $\text{Bi}_2\text{Se}_3$ ,  $\text{Bi}_2\text{Te}_3$ , *etc.* The exotic surface states of topological insulators are expected to form a playground of various topological quantum effects and show great potential in spintronics and quantum computation [16-18]. To fulfill the expectations, realizing topological insulator systems with significant surface transport is essential. However, due to the defects or impurities in the samples, it is extremely difficult to eliminate the bulk contribution to electron transport [19-24]. Up to date, there are no reliable transport measurements showing significant surface transport in current topological insulator systems despite extensive efforts involving chemical doping [22, 33-38], thin film or nanostructure fabricating [25-32], and electrical gating [21, 26, 32].

In this letter, we present strong evidences for significant surface transport in nanoflake devices of 200 nm thick topological insulator  $\text{Bi}_{1.5}\text{Sb}_{0.5}\text{Te}_{1.8}\text{Se}_{1.2}$  (BSTS). We have measured and compared electron transport behaviors between bulk single crystals and nanoflake devices of high quality BSTS, including the temperature dependence of resistivity and the angular and temperature dependence of the magnetoresistance

(weak antilocalization). The resistivity measurements show dramatic difference between nanoflake device and bulk single crystal in which the nanoflake device shows a transition from semiconductor to metal at 100 K with decreasing temperature, while the bulk crystal shows only semiconductor behavior in the measured temperature range from 300 K to 10 K. The resistivity of the nanoflake device is about 250 times smaller than that of the bulk single crystal. It is also found that the angle-dependent magneto-resistance curves in the nanoflake devices are fitted to a universal curve for the perpendicular component of an applied magnetic field. A fit to the two-dimensional weak antilocalization theory for the nanoflake device gives  $\sim T^{-0.51}$  dependence of the phase breaking length ( $< 200$  nm) on temperature  $T$  within 2 Tesla field. Furthermore, a time-dependent universal conductance fluctuation is observed in the nanoflake devices. All the experimental results suggest that significant surface transport has been realized in the three dimensional 200 nm thick nanoflake devices.

High quality BSTS single crystals are grown using modified Bridgeman methods. The obtained crystals are easily cleaved and reveal a flat and big shiny surface. Angle-resolved photoemission spectroscopy (ARPES) is performed with a VG Scienta R4000 electron analyzer at the SINS beamline at Singapore Synchrotron Light Source (SSLS). The angular and temperature dependent magnetoresistance of a 100  $\mu\text{m}$  thick bulk single crystal and 200 nm thick nanoflake devices are measured. The nanoflakes are mechanically exfoliated from the BSTS single crystal used for the

bulk transport measurement.

The resistivity is measured with the applied current in the (001) plane. The temperature dependence of the resistivity of the bulk and nanoflake samples measured in zero field are shown in Fig. 1a and Fig. 1b. The 100  $\mu\text{m}$  thick bulk crystal shows semiconductor behavior in the measured temperature regime and reaches a saturation behavior when  $T < 40$  K. The resistivity at 10 K is more than 200 times larger than that at room temperature. Although the nanoflake device also shows the semiconductor behavior in a high temperature range, the transport characteristics transfer to a metallic type when  $T < 150$  K. It should be noted from Fig. 1a and 1b that the resistivity of nanoflake is  $\sim 250$  times smaller than that of the bulk single crystal although the nanoflake is exfoliated from the bulk crystal used in the transport measurement (Fig. 1a). This indicates that the contribution from the surface states plays a more and more important role as the thickness reduces. Suppose the thickness of the surface states is 5 nm, we can easily conclude that the resistivity of the surface states is smaller than 1  $\text{m}\Omega\text{ cm}$  and the conductance contribution of the surface states is higher than 99% at 10 K. significant surface state transport can be realized when the nanoflake is several hundred nanometer thick. The inset of Fig. 1a shows the ARPES spectrum of the BSTS single crystal at room temperatures. The Dirac cone structure similar to the results in a very recent literature is observed [36]. The inset of Fig. 1b shows the morphology of the nanoflake device under Scanning Electron Microscopy.

To further confirm the two dimensional electron transport in the nanoflake device, we have performed the angular dependent magnetoresistance measurements. The magnetoresistance has been measured by tilting the bulk crystal and nanoflake device with respect to the applied magnetic field from  $0^\circ$  to  $90^\circ$ . The  $\theta = 0^\circ$  means the magnetic field parallel to the (001) surface while the  $\theta = 90^\circ$  means the magnetic field perpendicular to the (001) surface. Fig. 2a and 2b show the  $R(H)$  curves with various  $\theta$  for bulk single crystal and nanoflake device at 2K respectively. Both bulk and nanodevice show the weak antilocalization behavior in the low magnetic field region. Such a weak antilocalization at low temperature has been attributed to both strong spin-orbital coupling and topological  $\pi$  Berry phase of two dimensional surface states [39]. It is very obvious that  $\Delta R(H)/R(0)$  ratio decreases with decreasing  $\theta$  for both bulk single crystal and nanoflake device. The decrease of  $\Delta R(H)/R(0)$  with decreasing  $\theta$  is more pronounced for the nanoflake device. The variation of magnetoconductance for the bulk single crystal and nanoflake device in  $e^2/h$  unit as a function of the perpendicular component of the magnetic field are shown in Fig. 2c and 2d, respectively. All the  $G$  vs.  $B \sin \theta$  (the perpendicular component of the applied field) curves of the nanoflake device are merged into one universal curve, which strongly supports the significant surface state electron transport in the nanoflake BSTS. For the bulk single crystal, the magnetoconductance is due to both the surface state and the three dimensional bulk, therefore the  $G$  vs.  $B \sin \theta$  curve cannot be fitted to one universal curve. It is not a surprise that the weak antilocalization is observed for all

the angles in bulk because of the coexistence of both the bulk spin-orbit coupling effects and helical surface state contribution.

Magnetoconductances  $\Delta G = G(B) - G(0)$  at different temperatures (2 K, 4 K, 7 K, 10 K, 15 K, 35 K, and 40 K) have been measured in a the magnetic field perpendicular to the (001) plane ( $\theta = 90^\circ$ ), as shown in figure 3a and 3b for bulk single crystal and nanoflake device respectively. The Hikami-Larkin-Nagaoka (HLN) formula

$$\Delta\sigma_{2D} = \left[ -\frac{\alpha e^2}{2\pi^2\hbar} \right] \left[ \ln\left(\frac{\hbar}{4eL_\phi^2 B}\right) - \Psi\left(\frac{1}{2} + \frac{\hbar}{4eL_\phi^2 B}\right) \right]$$

is used to fit the magnetoconductance observed in both bulk and nanoflake device, where  $\Delta\sigma_{2D}$  is the two dimensional sheet conductance,  $\Psi$  is the digamma function,  $L_\phi$  is the phase breaking length, and  $\alpha$  is a prefactor which contains information about the nature of the electrons in topological insulators [40]. The fitted curves are plotted in Fig. 3(a) and 3(b) in solid lines. Due to the three dimensional bulk contribution, the fitting curves do not agree well with experiment data for bulk single crystal samples in the field up to 2 Tesla. For the nanoflake device, the two dimensional fitting curves agree very well up to 2 Tesla with the experimental data at all temperatures from 2 K to 45 K. The fitting results of  $L_\phi$  and  $\alpha$  for bulk single crystal and nanoflake device are shown in figure 3c, 3d, 3e, and 3f, respectively.

Due to the intermixing of bulk and surface states in bulk single crystal samples, the phase breaking length  $L_\phi$  and  $\alpha$  fitted by the two dimensional theory of weak antilocalization may not be able to reveal detailed physics, while the  $L_\phi$  and  $\alpha$  values

fitted from nanoflake device become reliable and illuminating. The phase breaking length  $L_\varphi \propto \sqrt{D\tau_\varphi}$ , where  $D$  is the diffusion coefficient and  $\tau_\varphi$  is the phase decoherence time or the mean time between inelastic events which is dependent on temperature. Generally,  $\tau_\varphi \propto T^{-p}$  where  $p = 1$  [41]. Thus, we use a power law to fit the collected temperature dependent  $L_\varphi$  and the fitting result is plotted in a red solid line in Fig. 3(d), which gives  $L_\varphi \propto T^{-0.51}$  for the nanoflake device. In two-dimensional electron-electron scattering system, the power law dependence should be  $T^{-1/2}$ . Hence, this is another evidence supporting that the origin of weak antilocalization features of device is from the surface states. It should be noted that the fitted  $L_\varphi$  at all temperatures are smaller than the thickness of the sample (200 nm), which strongly indicates that the two dimensional electron transport characteristics are due to the helical surface states. From this point of view, our experiment is very different from previous measurements on ultra-thin  $\text{Bi}_2\text{Se}_3$  and  $\text{Bi}_2\text{Te}_3$  films [26-31]. The two dimensional transport behavior in ultra-thin  $\text{Bi}_2\text{Se}_3$  and  $\text{Bi}_2\text{Te}_3$  films cannot be completely attributed to the surface states, because the  $L_\varphi$  is larger than the thickness of the film and therefore the film itself, including the bulk and surface states, form a two dimensional transport system. Since the thickness of our nanoflake BSTS device is larger than  $L_\varphi$ , it is a three dimensional transport system. The two dimensional transport behavior of weak antilocalization can only come from the helical surface states.

The coefficient  $\alpha$  takes a value of -1/2 for a traditional two dimensional electron

system with strong spin-orbit coupling. For the electron transport on one helical surface with a single Dirac cone,  $\alpha$  is also equal to  $-1/2$ . Since carriers on both up and bottom surface can contribute the conduction in topological insulator samples, double transport channels should add up to give  $\alpha = -1$ . In previous weak antilocalization studies in topological insulators, due to the ultra-thin film and large bulk contribution, the interactions between two surfaces and the intermixing of multiple conductance channels from bulk and surface bands at Fermi surface can introduce a correction which lead an  $\alpha$  different from  $-1$ . The experimental fitted  $\alpha$  covers a range between  $-0.4$  and  $-1.1$ . Our fitted  $\alpha$  at different temperatures is plotted in Fig 3(e) and (f). The fitted  $\alpha$  values deviate from  $-1$  for both bulk and nanoflake device at all temperatures. As the negative magnetoconductance behavior of bulk single crystalline BSTS cannot be fitted well using the two dimensional HLN formula, it is not a surprise that the fitted value is far away from the theoretical value of  $-1$ . For the nanoflake device, the fitting using HLN formula generates  $\alpha$  values between  $-0.7$  to  $-0.85$  for different temperatures. The deviation from  $-1$  may come from other effects, such as the warping of the Dirac cone.

We also observe a novel conductance fluctuation phenomenon in the nanoflake device under both low and high magnetic fields. The low magnetic field conductance fluctuation is very clear as shown in Fig. 2b and 2d. Fig. 4a shows the conductance fluctuations at different temperatures below 10 K between 4 and 9 Tesla perpendicular fields. Different from normal universal conductance fluctuations (UCF) discovered in

topological insulator  $\text{Bi}_2\text{Se}_3$  [22, 31], the conductance fluctuation in our nanoflake device evolves with time. Such time-dependent UCF can only be observed below 10 K and the magnitude of those fluctuations increases with decreasing temperature. The top 3 curves shown in Fig. 4 (a) were measured continuously with different field sweeping direction. As shown in the circled region in the figure, the curves show very similar fluctuation behaviors in the same magnetic field region because the time interval between the measurements is short. With the time evolution, the fluctuation patterns become different in the same magnetic field region. Time dependent UCF is due to the enhanced sensitivity of the conductance to the motion of individual scatters and such phenomena have been reported [42]. The variation of conductance pattern is due to the motion of scattering sites which changes the interference pattern of all the intersecting electronic paths in the coherent volume of the scattering sites. Since the motion of scattering sites is related to the time, the observed fluctuations are also time dependent which allows the non-retraceable results. As the electron transport in the nanoflake is almost fully surface transport as discussed before, the motion of the scattering site might be due to the time dependent surface contamination in the measurement chamber. Each magnetoresistance curve from 4 to 9 Tesla takes about 1 hour. According to the results, we can conclude that the scattering site pattern on the topological surface changes after about 30 minutes.

The amplitude of fluctuation detected is around  $0.2e^2/h$ . The phase decoherence length of electron  $L_\phi$  observed at 2 K is  $\sim 0.18 \mu\text{m}$  (Fig. 3d) and the thermal

length,  $L_T = \sqrt{\frac{\hbar D}{k_B T}}$  is around  $1\mu\text{m}$  at 2 K. As  $L_\varphi < L_T < L$ , the fluctuation of  $G$  can be calculated [43] as  $\delta G = \frac{e^2}{h} \left[ \frac{L_\varphi}{L} \right]^{4-d}$ , where  $L$  is the sample size. The calculated  $\delta G$  is  $0.3e^2/h$  which is quite close to our experiment data  $0.2e^2/h$  at 2 K. Furthermore, the root-mean-square (rms) of  $\delta G$  vs. temperature curve is also plotted as shown in Fig 4b. The rms of  $\delta G$  is usually following the power law  $rms\delta G \propto T^{-0.5}$  for two dimensional system. Our fitting shows  $rms\delta G \propto T^{-0.43}$ , which also indicates that the time-dependent UCF observed in the BSTS device sample is mainly from the surface states.

In conclusion, we demonstrate significant surface transport in single crystalline nanoflake devices of topological insulator BSTS. We have measured and compared electron transport behaviors between bulk single crystals and nanoflake devices, including the temperature dependence of resistivity and the angular and temperature dependence of the magnetoresistance. We observe weak antilocalization effect in both bulk single crystal and nanoflake devices. Further study shows that such phenomena origin from the surface states for nanoflake devices and intermixing of surface states and bulk spin-orbital couplings for bulk single crystals. A time dependent universal conductance fluctuation is observed in the nanoflake device. All the transport behaviors in nanoflake device strongly support the significant surface transport. The realization of significant surface states electron transport in nanoflake devices forms a perfect playground for future study of the electron and spin transport on topological

helical surface states.

Support for this work came from Singapore National Research Foundation (RCA-08/018) and MOE Tier 2 (MOE2010-T2-2-059).

- [1] L. Fu, C. L. Kane, and E. J. Mele, Phys. Rev. Lett. **98**, 106803 (2007).
- [2] J. E. Moore, Nature **464**, 194 (2010).
- [3] X. L. Qi and S. C. Zhang, Phys. Today **63**, 33 (2010).
- [4] M.Z. Hasan and C. L. Kane, Rev. Mod. Phys. **82**, 3045 (2010).
- [5] Y. Xia, D. Dian,, D. Hsieh, L. Wray, A. Pal, H. Lin, A. Bansil, D. Grauer, Y. S. Hor, R. J. Cava and M. Z. Hasan, Nat. Phys. **5**, 398 (2009).
- [6] Y. L. Chen, J. G. Analytis, J. H. Chu, Z. K. Liu, S. K. Mo, X. L. Qi, H. J. Zhang, D. H. Lu, X. Dai, Z. Fang, S. C. Zhang, I. R. Fisher, Z. Hussain, and Z. X. Shen, Science **325**, 178 (2009).
- [7] D. Hsieh, Y. Xia, L. Wray, D. Qian, A. Pal, J. H. Dil, J. Osterwalder, F. Meier, G. Bihlmayer, C. L. Kane, Y. S. Hor, R. J. Cava, and M. Z. Hasan, Science **323**, 919 (2009).
- [8] T. Hirahara, Y. Sakamoto, Y. Takeichi, H. Miyazaki, S. I. Kimura, I. Matsuda, A. Kakizaki, and S. Hasegawa, Phys. Rev. B **82**, 155309 (2010).
- [9] C Jozwiak, Y. L. Chen, A. V. Fedorov, J. G. Analytis, C. R. Rotundu, A. K. Schmid, J. D. Denlinger, Y. D. Chuang, D. H. Lee, I. R. Fisher, R. J. Birgeneau, Z. X. Shen, Z. Hussain, and A. Lanzara, Phys. Rev. B **84**, 165113 (2011).
- [10] D. Hsieh, Y. Xia, D. Qian, L. Wray, J. H. Dil, F. Meier, J. Osterwalder, L. Patthey, J. G. Checkelsky, N. P. Ong, A. V. Fedorov, H. Lin, A. Bansil, D. Grauer, Y. S. Hor, R. J. Cava, and M. Z. Hasan, Nature **460**, 1101 (2009).
- [11] A. Nishide, A. A. Taskin, Y. Takeichi, T. Okuda, A. Kakizaki, T. Hirahara, K. Nakatsuji, F. Komori, Y. Ando, and I. Matsuda, Phys. Rev. B **81**, 041309 (2010).
- [12] S. Souma, K. Kosaka, T. Sato, M. Komatsu, A. Takayama, T. Takahashi, M. Kriener, K. Segawa, and Y. Ando, Phys. Rev. Lett. **106**, 216803 (2011).
- [13] S. Y. Xu, L. A. Wray, Y. Xia, F. von Rohr, Y. S. Hor, J. H. Dil, F. Meier, B. Slomski, J. Osterwalder, M. Neupane, H. Lin, A. Bansil, A. Fedorov, R. J. Cava, and M. Z. Hasan, arXiv:1101.3985. (2011).
- [14] Z. Alpichshev, J. G. Analytis, J. H. Chu, I. R. Fisher, Y. L. Chen, Z. X. Shen, A. Fang, and A. Kapitulnik, Phys. Rev. Lett. **104**, 016401 (2010).
- [15] T. Zhang, P. Cheng, X. Chen, J.-F. Jia, X. C. Ma, K. He, L. L. Wang, H. J. Zhang, X. Dai, Z. Fang, X. C. Xie, and Q. K. Xue, Phys. Rev. Lett. **103**, 266803 (2009).
- [16] L. Fu and C. L. Kane, Phys. Rev. Lett. **100**, 096407 (2008).
- [17] X. L. Qi, R. Li, J. Zang, and S. C. Zhang, Science, **323**, 1184 (2009).
- [18] R. Yu, W. Zhang, H. J. Zhang, S. C. Zhang, X. Dai, and Z. Fang, Science **329**, 61 (2010).
- [19] J. G. Analytis, J. H. Chu, Y. Chen, F. Corredor, R. D. McDonald, Z. X. Shen, and I. R. Fisher, Phys. Rev. B **81**, 205407 (2010).
- [20] Y. S. Hor, A. Richardella, P. Roushan, Y. Xia, J. G. Checkelsky, A. Yazdani, M. Z. Hasan, N. P. Ong, and R. J. Cava, Phys. Rev. B **79**, 195208 (2009).
- [21] J. G. Checkelsky, Y. S. Hor, R. J. Cava, and N. P. Ong, Phys. Rev. Lett. **106**, 196801 (2011).
- [22] J. G. Checkelsky, Y. S. Hor, M.-H. Liu, D.-X. Qu, R. J. Cava, and N. P. Ong, Phys. Rev. Lett. **103** 246601 (2009).
- [23] N. P. Butch, K. Kirshenbaum, P. Syers, A. B. Sushkov, G. S. Jenkins, H. D. Drew, and J. Paglione, Phys. Rev. B **81**, 241301 (2010).
- [24] D. X. Qu, Y. S. Hor, J. Xiong, R. J. Cava, and N. P. Ong, Science **329** pp. 821 (2010).
- [25] H. Peng, K. Lai, D. Kong, S. Meister, Y. Chen, X.-L. Qi, S.-C. Zhang, Z.-X. Shen, and Y. Cui, Nat. Mater. **9**, 225 (2010).

- [26] J. Chen, H. J. Qin, F. Yang, J. Liu, T. Guan, F. M. Qu, G. H. Zhang, J. R. Shi, X. C. Xie, C. L. Yang, K. H. Wu, Y. Q. Li, and L. Lu, *Phys. Rev. Lett.* **105**, 176602 (2010).
- [27] Y. S. Kim, M. Brahlek, N. Bansal, E. Edrey, G. A. Kapilevich, K. Iida, M. Tanimura, Y. Horibe, S. W. Cheong, and S. Oh, *Phys. Rev. B* **84**, 073109 (2011).
- [28] M. Liu, J. Zhang, C. Z. Chang, Z. Zhang, X. Feng, K. Li, K. He, L. L. Wang, X. Chen, X. Dai, Z. Fang, Q. K. Xue, X. Ma, and Y. Wang, *Phys. Rev. Lett.* **108**, 036805 (2012).
- [29] M. Liu, C. Z. Chang, Z. Zhang, Y. Zhang, W. Ruan, K. He, L. L. Wang, X. Chen, J. F. Jia, S. C. Zhang, Q. K. Xue, X. Ma, and Y. Wang, *Phys. Rev. B* **83**, 165440 (2011).
- [30] H. T. He, G. Wang, T. Zhang, I. K. Sou, G. K. L. Wong, J. N. Wang, H. Z. Lu, S. Q. Shen, and F. C. Zhang, *Phys. Rev. Lett.* **106**, 166805 (2011).
- [31] S. Matsuo, T. Koyama, K. Shimamura, T. Arakawa, Y. Nishihara, D. Chiba, K. Kobayashi, T. Ono, C. Z. Chang, K. He, X. C. Ma, and Q. K. Xue, *Phys. Rev. B* **85**, 075440 (2012).
- [32] H. Steinberg, D. R. Gardner, Y. S. Lee and P. Jarillo-Herrero, *Nano Lett.* **10**, 5032 (2010).
- [33] Z. Ren, A. A. Taskin, S. Sasaki, K. Segawa, and Y. Ando, *Phys. Rev. B* **82**, 241306 (2010).
- [34] S. Jia, H. Ji, E. Climent-Pascual, M. K. Fuccillo, M. E. Charles, J. Xiong, N. P. Ong, and R. J. Cava, *Phys. Rev. B* **84**, 235206 (2011).
- [35] J. Xiong, A. C. Petersen, D. Qu, R. J. Cava, and N. P. Ong, arXiv:1101.1315 (2011).
- [36] T. Arakane, T. Sato, S. Souma, K. Kosaka, K. Nakayama, M. Komatsu, T. Takahashi, Z. Ren, K. Segawa, and Y. Ando, *Nat. Comm.* **3**, 636 (2012).
- [37] A. A. Taskin, Z. Ren, S. Sasaki, K. Segawa, and Y. Ando, *Phys. Rev. Lett.* **107**, 016801 (2011).
- [38] Z. Ren, A. A. Taskin, S. Sasaki, K. Segawa, and Y. Ando, *Phys. Rev. B* **84** 075316 (2011).
- [39] H. Z. Lu, and S. Q. Shen, *Phys. Rev. B* **84**, 125138 (2011).
- [40] E. McCann, K. Kechedzhi, V. I. Fal'ko, H. Suzuura, T. Ando, and B. L. Altshuler, *Phys. Rev. Lett.* **97**, 146805 (2006).
- [41] P. Santhanam, S. Wind, and D. E. Prober, *Phys. Rev. Lett.* **53**, 1179 (1984).
- [42] A. Trionfi, S. Lee, and D. Natelson, *Phys. Rev. B* **72**, 035407 (2005).
- [43] P. A. Lee, A. D. Stone, and H. Fukuyama, *Phys. Rev. B* **35**, 1039 (1987).

Figure captions:

Fig. 1. Temperature dependence of resistivity in zero field of (a) bulk single crystal with thickness of 100  $\mu\text{m}$  and (b) nanoflake device with thickness of 200 nm. The room temperature ARPES spectrum of BSTS single crystal and the morphology of the nanoflake device under Scanning Electron Microscopy (SEM) are shown in the insets of (a) and (b) respectively.

Fig. 2. Angle-dependent magnetoresistance/conductance of bulk BSTS single crystals and nano-device.  $\theta$  is the angle between the direction of the magnetic field and the current flow plane. (a) and (b) Magnetoresistance of bulk BSTS single crystal and BSTS nanoflake device at several  $\theta$ s under 2K respectively. (c) and (d) Magnetoconductance in unit of  $e^2/h$  vs. the perpendicular component of the magnetic field curves of bulk BSTS single crystal and BSTS nanoflake device respectively.

Fig. 3. Temperature-dependent magnetoconductance of BSTS single crystal and nanoflake device with  $\theta = 90^\circ$ . (a) Magnetoconductance change of bulk sample plotted with magnetic field at different temperatures in dot line. The 2D fitting curves are plotted in solid lines. The fitting curves do not agree with the experimental data well due to the intermixing effects. (b) The 2D WAL fitting curves agree very well up to 2 Tesla with the magnetoconductance change observed in nanoflake device at all temperatures from 2 K to 45 K. (c) and (d) The fitted values of  $L_\phi$  at different temperatures for single crystal and nanoflake device respectively. The fitting values follow the power law of temperature  $T^{-0.37}$  and  $T^{-0.51}$  respectively. (e) and (f) The fitted values of the prefactor  $\alpha$  at different temperatures for single crystal and nanoflake device respectively.

Fig 4 (a). Magnetofingerprint (UCF) signal  $\delta R$  vs magnetic field for the nanoflake device. At 2 K, we scan the field for three times with alternative field sweeping direction (the arrows). Seven UCF curves measured at temperatures between 2K to 10K were shown in the figures. (b) Temperature dependence of root mean square of the fluctuation of conductance. The solid line is the fitting curve using power law and the fitted power is -0.43.

Figure 1

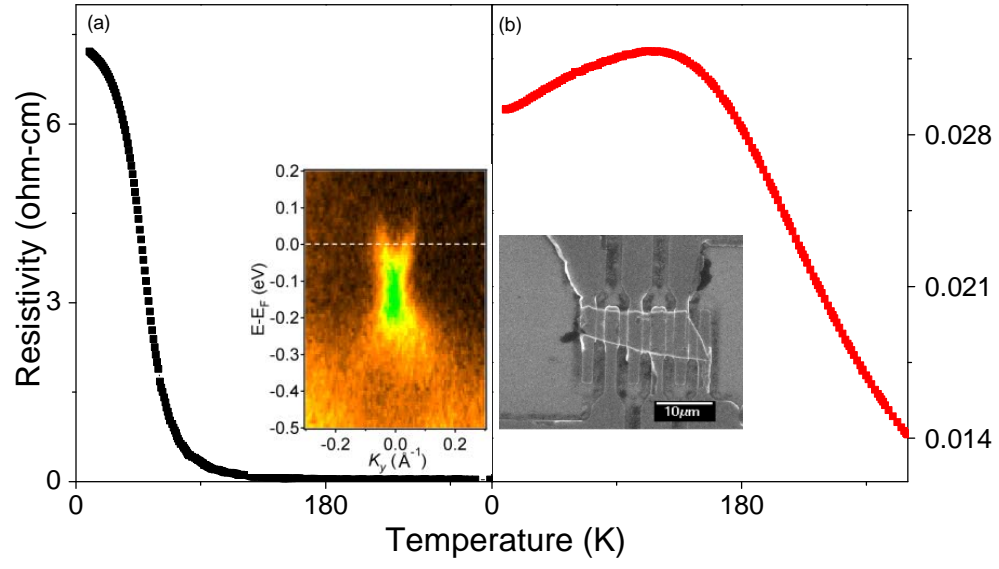


Figure 2

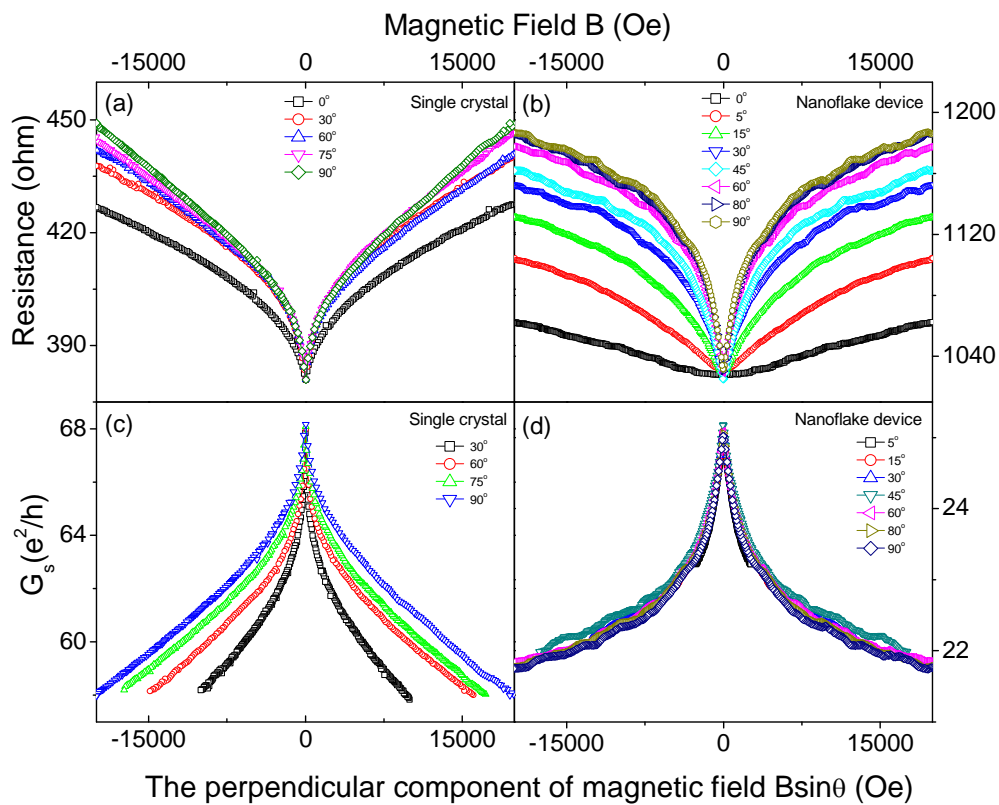


Figure 3

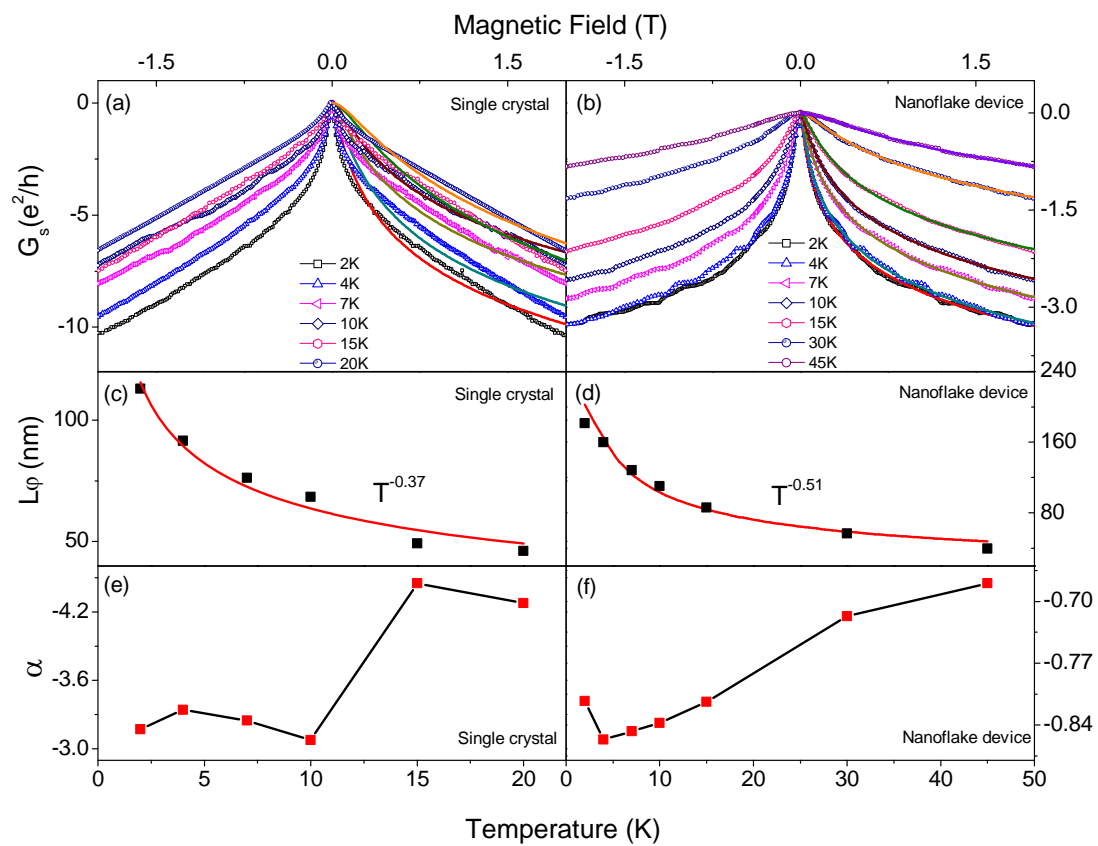


Figure 4

